Superelastic cellular NiTi tube-based materials: Fabrication, experiments and modeling

Guilherme Machado, Hervé Louche, Thierry Alonso, Denis Favier

▶ **To cite this version:**

Guilherme Machado, Hervé Louche, Thierry Alonso, Denis Favier. Superelastic cellular NiTi tube-based materials: Fabrication, experiments and modeling. Materials & Design, 2015, 65, pp.212-220. 10.1016/j.matdes.2014.09.007 . hal-01285370

HAL Id: hal-01285370
https://hal.science/hal-01285370

Submitted on 11 Mar 2016

HAL is a multi-disciplinary open access archive for the deposit and dissemination of scientific research documents, whether they are published or not. The documents may come from teaching and research institutions in France or abroad, or from public or private research centers.

L'archive ouverte pluridisciplinaire **HAL**, est destinée au dépôt et à la diffusion de documents scientifiques de niveau recherche, publiés ou non, émanant des établissements d'enseignement et de recherche français ou étrangers, des laboratoires publics ou privés.

Superelastic cellular NiTi tube-based materials: fabrication, experiments and modeling

G. Machado*[,a,b], H. Louche[a], T. Alonso[b], D. Favier[b]

[a] *LMGC, CNRS-Université de Montpellier 2, Place E. Bataillon CC048, 34095 Montpellier, France*
[b] *UJF-Grenoble1, CNRS, TIMC-IMAG - UMR5525, Grenoble, France.*

Abstract

The aim of this paper is to present an experimental and modeling study as the first step towards designing and optimizing architectured materials constituted of NiTi tubes. The idea is to combine the intrinsic and novel properties of nickel-titanium shape memory alloys with purposely engineered topologies. By joining thin-wall superelastic tubes via electrical resistance welding, we create regular cellular material demonstrators. The superelastic behavior of two simple architectured materials based on identical tubes, but with two topologies, are experimentally characterized and modeled using finite element approaches. The predicted behaviors are compared by simulating complex loading, exploring the influence of the constitutive material behavior on the effective mechanical properties of cellular materials. The parameters of the constitutive equations are identified on tensile tests performed on small dog-bone shaped specimens, machined from the tubes by spark cutting. The modeling results are finally compared with compression tests performed on these simple architectured NiTi materials. As a further validation of the proposed study, two large cell structures (square and hexagonal stacking) were modeled to gain greater insight into the role of different architectures.

Key words: NiTi Shape Memory Alloy; NiTi tubes; resistance welding; architectured material;

1. Introduction

Nickel-titanium (NiTi) shape memory alloys (SMA) have been used in a wide variety of consumer products and industrial applications; such as in automotive [1], aerospace [2], biomedical [3] and many other potential industrial commercial markets [4] due to their remarkable superelastic properties, shape memory effects, and biocompatibility. These

*Corresponding author
Email address: guilherme.machado@imag.fr (G. Machado)
[1]Phone: +33456520086 Fax: +33476768844

alloys can withstand more than 8 % strain during a superelastic tensile test with practically full recovery of all this deformation during unloading. This leads to a highly non-linear stress-strain curve that includes hysteresis.

Despite being widely used in a broad range of industries, the implementation of NiTi in structural applications can be expensive and complex due to limitations in traditional fabrication processes, e.g., machining [5] and casting [6]. More so than other materials, NiTi SMA properties are significantly affected by the fabrication processes [7]. Given the difficulties in obtaining and manufacturing NiTi parts associated with the fact that the most widely manufactured commercial shapes are round cross-sectional wires and bars, tubes and small rectangular cross-sectional strips, one of the solutions to address this challenge is to develop an architectured material.

Architectured materials are combinations of two or more materials or of materials and void, having a controlled architecture at different length scales, and configured in such a way as to have attributes not offered by any bulk material alone [8]. Fig. 1 shows examples of architectured materials.

There have been several attempts to fabricate SMA architectured materials using basic commercial shapes. Grummon *et al.* [9] developed a novel brazing technique that allowed creation of prototypes of superelastic cellular honeycomb topologies from conventional NiTi precursor materials such as corrugated sheets (Fig. 1a). In a similar manner, after shape-setting the honeycomb foil shape, Okabe *et al.* [10] designed a sandwich panel where NiTi foils of honeycomb core were glued using a modified silicone adhesive. Hassan *et al.* [11] used mechanical fasteners to construct a prototype of a smart SMA chiral honeycomb using NiTi ribbons (Fig. 1b). Various combinations of SMAs and other materials have improved the material performance such as triple-state changing effect presented in [12] combining SMA wires and shape memory polymer matrix. Marcadon *et al.* [13] presented another interesting study exploring the influence of the constitutive material behavior on the effective mechanical properties of brazed cellular materials using tubes made of Inconel® 600.

The present paper discusses the fabrication, testing, and finite element analysis of superelastic cellular NiTi tube-based materials. These cellular structures made from welded tubes are especially interesting for their potential to provide superelasticity and shape memory in a light-weight material. Nevertheless, they can be designed to have high stiffness-to-mass ratios and desirable energy absorption characteristics since their stress-strain curves may exhibit large hysteresis loops. Multi-tube structures allow combination

of different diameter-wall thickness ratios and stacking topologies. The structure effect, by exploiting wall bending, can substantially amplify the SMA intrinsic properties as compared with the monolithic SMA volume. In this context, Section 2 starts with a brief description of resistive welding, where the set-up and fabrication of two demonstrators of cellular structures are outlined. In Section 3, all precautions concerning the experimental set-up are emphasized and an analysis is conducted concerning the thermal transformation behavior of the received material. In the same section, mechanical tests are divided into three categories: (1) uniaxial tensile tests; (2) single tube under radial compression by flat loading surfaces and (3) two cellular demonstrators under compression. In Section 4, experimental data are compared to a finite element model carried out using a SMA mechanical model fitted only on uniaxial tensile tests. Based on previous results, two large cell structures (square and hexagonal stacking) were modeled to gain grater insight into the role of different architectures. Finally, Section 5 contains some concluding remarks and outlines some future perspectives.

2. Tube stacking specimen fabrication

Electrical resistance welding was used as technique to join NiTi stacked tubes. Analysis of the experimental evidence presented in [14] demonstrates that resistance welding is a feasible technique for joining NiTi tubes for the design and creation of complex structures with high reversible elasticity.

In this study, NiTi tubes were provided by Minitubes (Grenoble, France), with a nominal composition of Ti-50.8 at.% Ni. Tubes were obtained by the cold drawing process. The end tube dimensions are the result of a series of drawing passes through different die/mandrel sizes in order to progressively reduce the inner and outer diameters [15, 16]. The tube has an outer diameter of $\phi_{ext} = 5.74\,\text{mm}$ and a wall thickness of $t = 0.31\,\text{mm}$. From as-received cold-worked tubes, tubular samples of $l = 5\,\text{mm}$ length were cut using a diamond saw.

A DC Hughes Model VTA-60 resistance welder was used. The welding set-up is illustrated in Fig. 2. Two cylindrical copper electrodes of 4 mm diameter and 20 mm long were used to clamp the tubular samples together. A plexiglas template ensured the tube position and alignment. Resistance welding was carried out in an argon atmosphere using an electrical pulse energy of $E = 145\,\text{J}$ and a contact force of $F = 100\,\text{N}$. Each weld was done in a single step. The weld line was well distributed along the length of the tube and approximately 0.5 mm wide, observed in a scanning electron microscope. Two cellular

structures, named here square (Fig. 7a) and triangular (Fig. 8a), were fabricated and aged at $T = 350\,^{\circ}\mathrm{C}$ for 60 min after welding. For further details on the effect of aging treatment on the transformation behavior and on deformation behavior of Ni-rich alloys, see [17] and [18].

3. Experimental results and Analysis

3.1. Thermal transformation behavior

The thermal transformation behavior of cold-worked material and samples aged at $350\,^{\circ}\mathrm{C}$ for 60 min were determined by differential scanning calorimetry, using a DSC Q200 V24.4 instrument. The heating and cooling rates were set at $10\,^{\circ}\mathrm{C/min}$. All measurements started with heating from $T = 40\,^{\circ}\mathrm{C}$. Fig. 3 shows the DSC curves of the cold-worked and the aged samples for two different zones. Fig. 3a was obtained with DSC specimens taken far from the welded joint. Fig. 3b represents DSC specimens in the welded joint. Thus, four different states are defined: *state 1*, the cold-worked material; *state 2*, the aged material; *state 3*, the welded zone before aging; *state 4*, the welded zone after aging. For *state 1*, the peaks have a low intensity. This is consistent with previous studies for cold-worked NiTi [19, 20]. *State 2* exhibits flat but distinguishable A-to-R during cooling and R-to-A during heating transformation peaks above room temperature. The R-to-M and M-to-R transformations are undetectable due to their extremely low intensities or their low temperatures. Concerning *states 3* and *4* nothing can be precisely concluded since the DSC samples are not homogeneous over the welded zone. The austenite finish temperature (A_f) was determined to be under $60\,^{\circ}\mathrm{C}$ in all states.

3.2. Uniaxial tensile tests

In order to determine the mechanical behavior of tube specimens, uniaxial tensile tests were performed on small dog-bone shaped specimens machined from the tubes by spark cutting. The samples had an initial gage length $l_0 = 6\,\mathrm{mm}$, width $w_0 = 0.8\,\mathrm{mm}$ and thickness $t_0 = 0.31\,\mathrm{mm}$, as shown in Fig. 4. All tests on the following were performed using a Gabo Explorer testing machine with a $\pm 500\,\mathrm{N}$ load cell and with specially designed grips. The testing temperature was controlled using a furnace in air with fanned convection with an accuracy of $\pm 1\,^{\circ}\mathrm{C}$. In all cases, the testing temperature was approached by cooling from a temperature higher than $60\,^{\circ}\mathrm{C}$. Test images were recorded at 10 Hz with a Jai TM-4200GE CCD 1024×1024 pixel camera and the spatial resolution achieved for digital image correlation (DIC) was 0.05 mm. Strain was calculated by averaging the strain field over the gage zone. The tests were performed at a global strain rate of

$10^{-5}\,s^{-1}$. Strain fields were calculated for the sequence of images corresponding to loading and unloading. Fig. 5a shows the nominal stress-strain first load-unload curves of the uniaxial sample tested at 60, 70 and 80 °C. The effect of the testing temperature on critical stresses for the forward and the reverse transformations was found to follow the Clausius-Clapeyron relationship with a slope close to 6.5 MPa/°C. The samples tested above 60 °C demonstrated pseudoelastic behavior, recovering any minor remaining deformation upon heating. Fig. 5b shows the transformation and plastic strain until failure at 60 °C for a sample aged at 350 °C for 60 min (MAT1), with the sample solution treated at 850 °C for 60 min followed by a 350 °C for 60 min aging (MAT2). Note that results were expressed in terms of logarithm and Green-Lagrange strains measures and their respective stresses. These results will be used to model the plastic behavior of tubes. For simplicity, we assume negligible temperature effects in the plastic hardening curves. The uniaxial behavior of MAT2 will be used to approximate the mechanical behavior of welded zones (WZs). Indeed, as pointed out in [14], the microstructures of a heat treated (solution treated and aged) and weld fusion zone are very similar. They contain large grains with almost identical shape and size.

3.3. Radial compression test of a single tube

Research on the large deformation behavior of NiTi tubes under quasi-static radial compression is not new in the literature. This type of test was used, for example, by [21] in the design of passive vibration isolation. [22] performed radial compression of tubes with different diameter-wall thickness ratios (ϕ_{ext}/t). They highlighted the "giant superelasticity effect", that combines the geometry effect, expressed by the ϕ_{ext}/t ratio, and the intrinsic properties of NiTi SMA. [23] conducted a systematic investigation on deformation behavior and influences of geometric dimensions for different boundary constraints.

In the present work, tubular samples of $l = 5$ mm length were radially loaded between steel platens without lubrication. The lower head was fixed and the upper one was the loading head moving at 0.1 mm/s. Force and displacement sensors recorded the force-displacement curves, presented in Fig. 6, at 60 and 70 °C.

3.4. Radial compression test of tube stackings

Compressive quasi-static loading was applied to the tube stacking with a constant crosshead velocity of 0.1 mm/s. Three loading-unloading cycles were successively performed at 4 %, 8 % and 12 % global strain ($\varepsilon_g = \Delta H/H_0$) for both cellular structures. No damage of welded zones (WZs) was observed at this deformation level. Stress concentration and localized plasticity phenomena induced by the stacking geometry could result

in different and more complex material behavior for tube stackings compared to single tubes. Figs. 7 and 8 present the undeformed configuration and deformed shapes recorded by a visible CCD camera at $T = 23\,^{\circ}\mathrm{C}$. The deformation mode for the square sample is symmetric with respect to the vertical and horizontal axes, whereas the triangular sample is symmetric only with respect to the vertical axis, and the deformation appears to be concentrated on the upper tube.

Fig. 9 shows the load-deformation curves for the two samples before weld damage for three temperatures. The maximum global compression strain imposed is 12% in both cases. Stiffness is higher for the square sample than for the triangular one, whereas the hysteretic loops are quite similar.

4. Finite element simulations

4.1. Modeling of the experimental results

Nonlinear finite element simulations were performed to analyze the deformation behavior of NiTi tube structures. The Abaqus commercial finite element code was used with a user material routine (UMAT) that follows the model proposed by [24]. This constitutive model reproduces some basic features of shape-memory alloys at finite strains. The model is based on an additive strain decomposition in which the total strain is taken as the sum of the elastic strain, the transformation strain, and the plastic strain. Plastic strains develop as soon as the material is loaded beyond full transformation. The work-hardening behavior is assumed to exhibit tension-compression symmetry. A comprehensive treatment would require knowledge of the complete yield envelope and the work-hardening characteristics as a function of the stress state.

The material data required by the model are obtained only from observations of the uniaxial tensile tests performed in Section 3.2. The data characterize the start and end of the phase transformation during loading, unloading and reverse loading. The different elastic constants for the austenite and martensite phases are taken into account. Temperature effects are included as well. In this work, no volumetric transformation strains are considered. Many authors [25, 26, 27] have found asymmetries of transformation stress and transformation strain between tension and compression. The start of transformation stress during loading in compression, is reported to be around 30% greater than start of transformation stress during loading in tension. For comparison, the tension-compression asymmetry is considered only in the single tube model. Table 1 presents two sets of parameters to model the material for the tube wall (MAT1) and the welded zone material

(MAT2), respectively. Table 2 presents the stress-strain points that define the yield curves. All parameters are expressed in terms of Cauchy stress and logarithm strain measure.

Fig. 10a compares the finite element predicted curves to the experimental uniaxial tensile tests. A good match with the experimental data is obtained when the temperature effects are included. A continuum 8-node biquadratic plane strain fully integrated element (CPE8) was used for single tube, square and triangle models. The mesh sensitivity was first assessed by running multiple simulations with gradual mesh size refinement. The mesh size was selected after which the results showed mesh independence. All elements were chosen to be close to a square, insofar as possible, in undeformed configuration. For all subsequent analysis 18 Gauss integration points over the tube thickness were used. This ensured that the results were independent of the mesh geometry even though some small differences can be noted at singular points. A flat analytical rigid surface was used to represent the compression platens. The hard contact pressure-overclosure relationship was used to define the finite-slide contact interaction between platens and tubes. Zero-penetration condition was enforced by an augmented Lagrange iteration scheme that drives down the penetration distance. For simplicity, a frictionless behavior is assumed. These same contact settings were used to define the self-contact between neighboring tubes during stacking compaction.

Simulation results for a single tube compression (Fig. 10b) and both architectures, i.e., square (Fig. 10c) and triangle (Fig. 10d), are also superimposed with the experimental data. It is noted that the predicted results for a single tube compression (Fig. 10b) were stiffer than the experimental curve. This difference further increased when a tension-compression dissymmetry of 20% was considered. The difference between experimental and model results could be explained by the fact that undeformed tubes did not have a perfectly cylindrical shape (straightness imperfections). Then the contact surface of the tube, especially in the first load increments (until 5%), was not uniform. The effects of this type of small imperfection tended to decrease, i.e., to be averaged when more tubes were added, as in the case of the Figs. 10c and 10d. Even with all precautions taken to align tubes during welding, a small discrepancy resulting from tube misalignment can also occur. On one hand, work on small samples increases the sensitivity to defects and makes the comparison between the modeling and experimental results more difficult. On the other hand, it is important to keep in mind the simplicity of the constitutive model. Fig. 10 shows relatively close agreement between the experimental data and FEA predictions for all cases. However, for larger strain levels, the predicted hysteresis overestimated the

experimental hysteresis.

These first results provide information on the respective contributions of both constitutive material properties and architecture of the cellular structure on its effective behavior. The balance between these two contributions varies according to deformation level and the type of architecture.

4.2. Role of the modeling in the design of superelastic cellular NiTi tube-based materials

In order to illustrate the possibility of using the previous results to gain a grater insight into the role of the architecture and boundary conditions, two large cell structures shown in Figs. 11 and 12 are modeled: a 6×6 square stacking and a $5(4)\times6(3)$ hexagonal stacking, containing approximately the same number of tubes. The influence of boundary conditions was also evaluated using two different compression platen geometries. In the first load case, flat platens were modeled by an analytical rigid surface, as shown in Fig. 11. In the second load case, an analytical rigid surface composed of semicircles was used to model grooved platens, as shown in Fig. 12. The compression mechanical responses of square and hexagonal stackings, with the two different loading cases, are plotted in Fig. 13.

Due to symmetry, only one-quarter of the stackings were simulated, while applying planar boundary conditions on symmetrical faces. The results were mirrored in the symmetry planes. Figs. 11a, 11b, 12a and 12b show the undeformed configurations (in solid lines) and the deformed configurations (Mises equivalent stress field) under imposed displacement, resulting in 5% of global strain in all cases. The computed deformed shapes exhibited a stress concentration along the weld fillet. No adaptive remeshing procedure was applied.

For the first load case (flat platens), no horizontal forces occurred in the square staking (Fig. 11a) since no friction was considered. The maximum strain of $\varepsilon_g = 5\%$ was not sufficient to activate phase transformation. Thus, no hysteresis was observed in the force vs. global strain curve in Fig. 13. In the hexagonal structure (Fig. 11b), the upper and lower layers moved horizontally, causing a strong deformation localization on these layers.

In the second load condition (grooved platens), Fig. 12a shows that square stacking attained a barrel shape. This was due to horizontal forces which were not constant over the entire cross section of the specimen. However, a more uniform force distribution on the tube-wall network was obtained for hexagonal stacking using grooved platens.

The modeling results show that a more uniform force distribution was obtained using flat platens for the square stacking and grooved platens for the hexagonal stacking. Considering the compression mechanical behavior in Fig. 13, both architectures are fully

recovered after load removal. This suggests that most of the integration points are in the pseudo-elastic regime. It is interesting to note that the hexagonal stacking is stiffer than the square one for both load cases. This is in agreement with previously reported data [13] for a different constitutive material. In addition, higher hysteresis is obtained with hexagonal stacking.

The analysis was then extended by isolating a single tube from each architecture considering the second load case using grooved platens. Figs. 12c and 12d show, in detail, the equivalent strain in these tubes chosen near to the symmetry planes. This precaution is especially necessary to avoid border effects and ensure a periodic circumferential strain distribution. The results shown in Figs. 12c and 12d suggest that the numbers of martensitic transformation hinges (THs) are equal to the number of WZs and they are located symmetrically on the circumference of the tube. Comparing both architectures, it is possible to observe that when the number of WZs increases over the tube circumference the arc-length of cell wall decreases, causing the structure to become stiffer. At the same time, it also increases the level of cell wall bending.

The contour plot of the equivalent strain is shown in Figs. 12c and 12d at the moment of maximum global strain ($\varepsilon_g = 5\%$). In the square stacking, the maximum strain is less than 5%. Only a few parts of the tube near WZs experienced a phase transition and THs were not fully developed. For the same global strain level, the hexagonal stacking shows a maximum local strain of about 8.15% in WZ_2 and WZ_5. Six THs seem to be formed, but only four (TH_2, TH_3, TH_5 and TH_6) show local strains greater than the transformation strain $\varepsilon^l = 0.04$ defined in Table 1. In both architectures, no plasticity was induced since the local strains were less than those that define the beginning of the yield curve in Table 2.

Figs. 12c and 12d reveal that bending deformation can also activate stress-induced martensitic phase transformation in WZs. This effect is more evident in certain WZs: WZ_1 and WZ_3 for square stacking and WZ_2 and WZ_5 for hexagonal stacking. Otherwise, transformation can be attributed to stress concentration on the WZs neighborhood: WZ_2 and WZ_4 for square stacking and WZ_1, WZ_3, WZ_4 and WZ_6 for hexagonal stacking. This suggests that the geometrical disposition between WZs and THs zones as well as the martensite volume fraction of each zone are important. Thus, some welded zones can also contribute with the overall structure hysteresis.

5. Conclusions

Modeling is very useful for designing and optimizing architectured materials. In this paper, the mechanical superelastic behavior of NiTi architectured tube-based NiTi materials subjected to quasi-static compression was studied using two simple cellular samples. This study demonstrated that resistance welding is a feasible technique to obtain architectured materials consisting of NiTi with low density and high reversible pseudo-elasticity. All the samples can practically recover their initial shape during unloading in the experimental load range, and the load-displacement curves appear as hysteretic superelastic loops, which are related to reversible austenite-martensite phase transformation. These first results provide information on the respective contributions of the constitutive material properties and architecture of the cellular structure on its effective behavior. The balance between these two contributions varies according to the stress-strain level. Further work to optimize the architecture, thermal treatment and process parameters is ongoing using the experimental and modeling approaches described in the present paper.

Acknowledgment

The authors wish to acknowledge the financial support of the French ANR research program ANiM: Architectured NiTi Material (N.2010 BLAN 90201).

References

[1] Stoeckel D. Shape memory actuators for automotive applications. Mater Des 1990;11:302–7.

[2] McDonald Schetky L. Shape memory alloy applications in space systems. Mater Des 1991;12:29–32.

[3] Morgan N. Medical shape memory alloy applicationsthe market and its products. Mater Sci Eng, A 2004;378:16–23.

[4] Mohd Jani J, Leary M, Subic A, Gibson MA. A review of shape memory alloy research, applications and opportunities. Mater Des 2014;56:1078–113.

[5] Weinert K, Petzoldt V. Machining of NiTi based shape memory alloys. Mater Sci Eng, A 2004;378:180–4.

[6] de Araújo C, da Silva N, da Silva M, Gonzalez C. A comparative study of Ni–Ti and Ni–Ti–Cu shape memory alloy processed by plasma melting and injection molding. Mater Des 2011;32:4925–30.

[7] Wu M. Fabrication of nitinol materials and components. In: Materials Science Forum. Trans Tech Publication 2002;394:285–92.

[8] Ashby M. Designing architectured materials. Scripta Mater 2013;68:4–7.

[9] Grummon DS, Shaw JA, Foltz J. Fabrication of cellular shape memory alloy materials by reactive eutectic brazing using niobium. Mater Sci Eng, A 2006;438-440:1113–8.

[10] Okabe Y, Minakuchi S, Shiraishi N, Murakami K, Takeda, N. Smart honeycomb sandwich panels with damage detection and shape recovery functions. Adv Compos Mater 2008;17:41–56.

[11] Hassan M, Scarpa F, Ruzzene M, Mohammed N. Smart shape memory alloy chiral honeycomb. Mater Sci Eng, A 2008;481:654–7.

[12] Ghosh P, Rao A, Srinivasa AR. Design of multi-state and smart-bias components using shape memory alloy and shape memory polymer composites. Mater Des 2013;44:164–71.

[13] Marcadon V, Davoine C, Passilly B, Boivin D, Popoff F, Rafray A, Kruch S. Mechanical behaviour of hollow-tube stackings: Experimental characterization and modelling of the role of their constitutive material behaviour. Acta Mater 2012;60:5626–44.

[14] Delobelle V, Delobelle P, Liu Y, Favier D, Louche H. Resistance welding of NiTi shape memory alloy tubes. J Mater Process Tech 2013;213:1139–45.

[15] Palengat M, Chagnon G, Favier D, Louche H, Linardon C, Plaideau C. Cold drawing of 316L stainless steel thin-walled tubes: Experiments and finite element analysis. Int J Mech Sci 2013;70:69–78.

[16] Linardon C, Favier D, Chagnon G, Gruez B. A conical mandrel tube drawing test designed to assess failure criteria. J Mater Process Tech 2014;214:347–57.

[17] Zhenga Y, Jianga F, Li L, Yang H, Liu Y. Effect of ageing treatment on the transformation behaviour of Ti–50.9 at.% Ni alloy. Acta Mater 2008;56:736–45.

[18] Jiang F, Liu Y, Yang H, Li L, Zheng Y. Effect of ageing treatment on the deformation behaviour of Ti–50.9 at.% Ni. Acta Mater 2009;57:4773–81.

[19] Frick CP, Ortega AM, Tyber J, Maksound A, Maier HJ, Liu Y, Gall K. Thermal processing of polycrystalline niti shape memory alloys. Mater Sci Eng, A 2005;405:34–49.

[20] Sharifi EM, Karimzadeh F, Kermanpur A. The effect of cold rolling and annealing on microstructure and tensile properties of the nanostructured Ni50Ti50 shape memory alloy. Mater Sci Eng, A 2014;607:33–7.

[21] Khan MM, Mayes JJ, Systems A, Helicopter B, Worth F, Henderson BK. Pseudoelastic SMA spring elements for passive vibration isolation, Part I: Modeling. J Intel Mater Sys Str 2004;15415–41.

[22] Rivin E, Sayal G, Johal P. Giant superelasticity effect in NiTi superelastic materials and its applications. J Mater Civil Eng 2006;18:1–7.

[23] Ke Z, Huijie Z, Zhiping T. Experimental study of thin-walled NiTi tubes under radial quasi-static compression. J Intel Mater Sys Str 2001;22:2113–26.

[24] Auricchio F, Taylor R. Shape-memory alloys: modelling and numerical simulations of the finite-strain superelastic behavior. Comput Methods Appl Mech Eng 1997;143:175–94.

[25] Orgéas L, Favier D. Stress-induced martensitic transformation of a NiTi alloy in isothermal shear, tension and compression. Acta Mater 1998;46:5579–91.

[26] Lim T, McDowell D. Mechanical behavior of an Ni-Ti shape memory alloy under axial-torsional proportional and nonproportional loading. J Eng Mater Tech 1999;121:9–18.

[27] Gall K, Sehitoglu H. The role of texture in tension-compression asymmetry in polycrystalline NiTi. Int J Plast 1999;15:69–92.

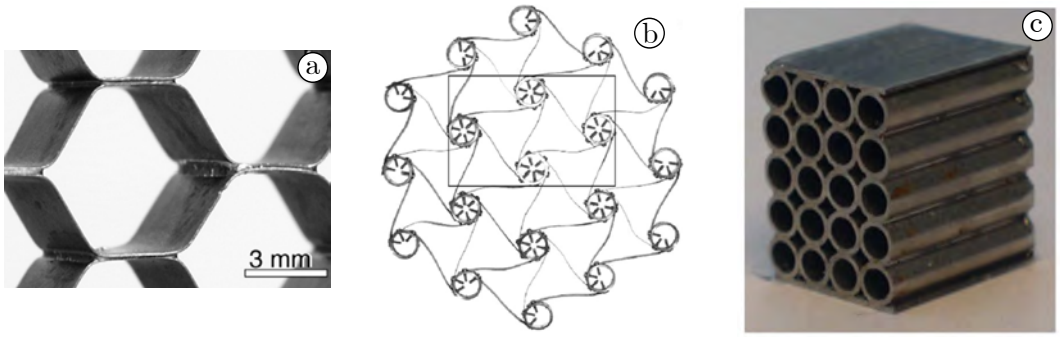

Figure 1: Some architectured material examples: (a) superelastic Nitinol honeycomb structure [9]; (b) SMA chiral honeycomb using NiTi ribbons [11]; and (c) Inconel® 600 architectured cellular material processed using a brazing heat treatment [13].

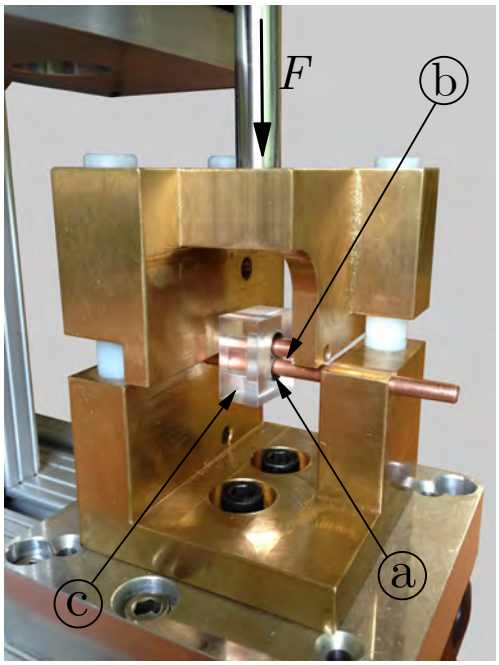

Figure 2: Tube welding set-up: (a) tubes; (b) cylindrical copper electrodes; and (c) Plexiglas template.

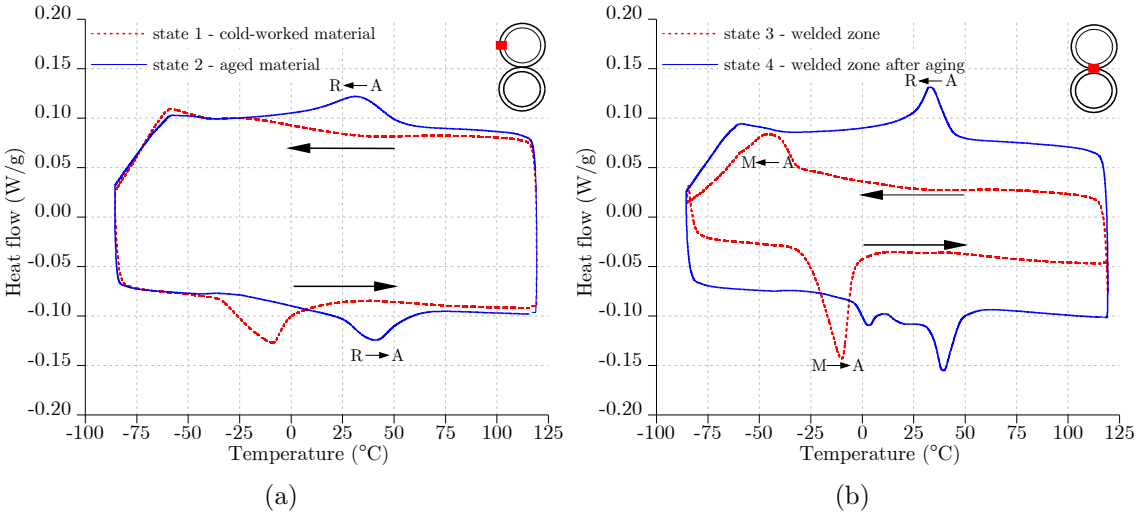

Figure 3: Thermal transformation behavior of Ti-50.8 at.% Ni for (a) zone far from the welded joint and (b) welded zone. In both cases, samples were examined before and after aging treatment at 350 °C for 60 min.

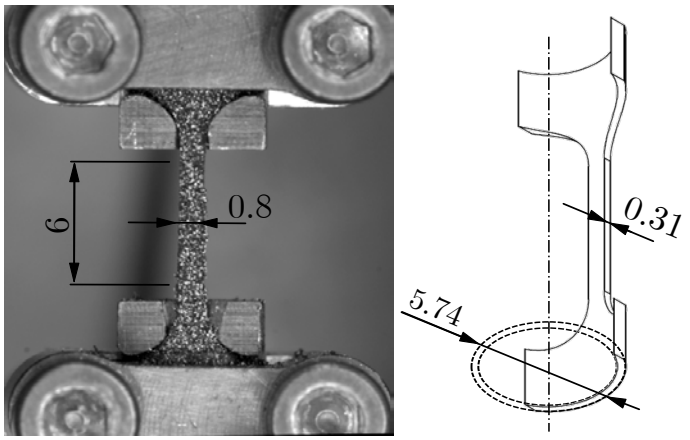

Figure 4: Uniaxial tensile specimen machined from tubes by spark cutting (dimensions in mm).

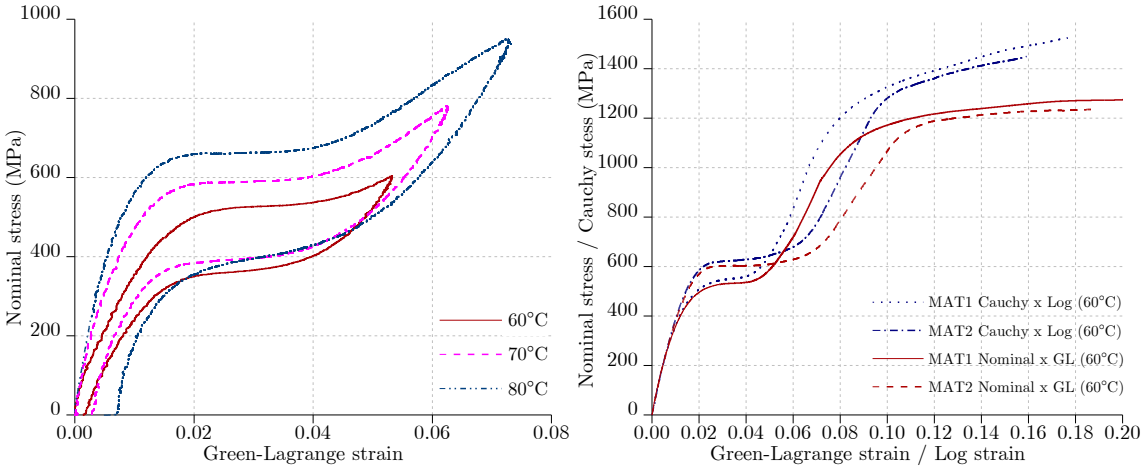

Figure 5: Nominal stress-strain curves resulting from tensile tests: (a) influence of the test temperature during loading and unloading at $T = 60, 70$ and $80\,^{\circ}\mathrm{C}$; (b) Ultimate tensile strength at $60\,^{\circ}\mathrm{C}$ for the specimen aged at $350\,^{\circ}\mathrm{C}$ for 60 min (MAT1) and specimen solution treated at $850\,^{\circ}\mathrm{C}$ for 60 min followed by $350\,^{\circ}\mathrm{C}$ for 60 min aging (MAT2).

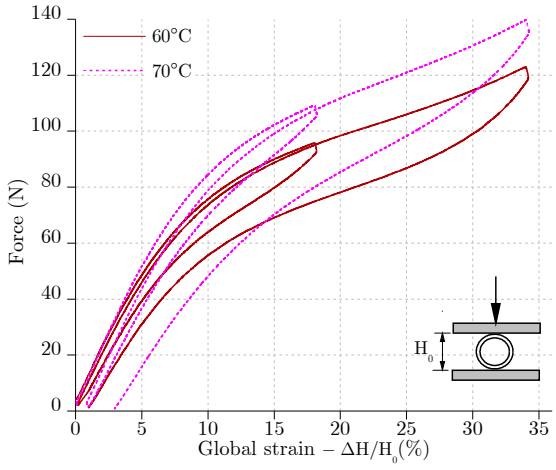

Figure 6: Force vs. global strain ($\varepsilon_g = \Delta H/H_0$) response at $T = 60\,^{\circ}\mathrm{C}$ and $70\,^{\circ}\mathrm{C}$ of radially loaded superelastic NiTi tube $\phi_{ext} = 5.74\,\mathrm{mm}$ at a loading rate $0.1\,\mathrm{mm/s}$.

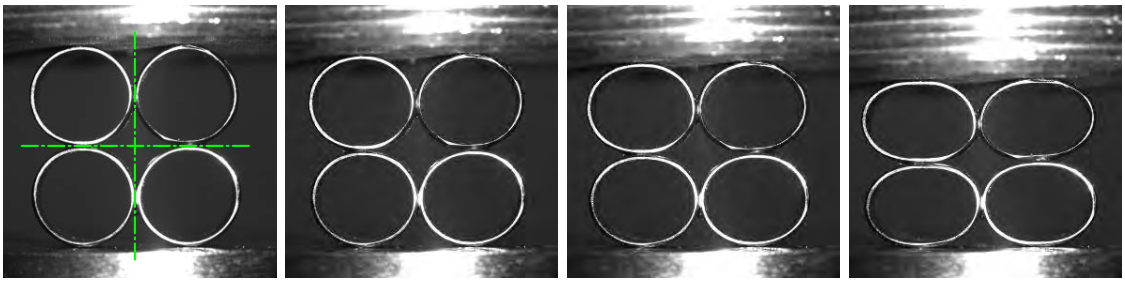

(a) (b) (c) (d)

Figure 7: Visible CCD images of a square sample at $T = 23\,^{\circ}\mathrm{C}$ under quasi-static compression at a loading rate of 0.1 mm/s. (a) undeformed configuration with initial length $H_0 = 11.48\,\mathrm{mm}$,(b) $\varepsilon_g = 4\,\%$, (c) $\varepsilon_g = 8\,\%$ and (d) $\varepsilon_g = 12\,\%$.

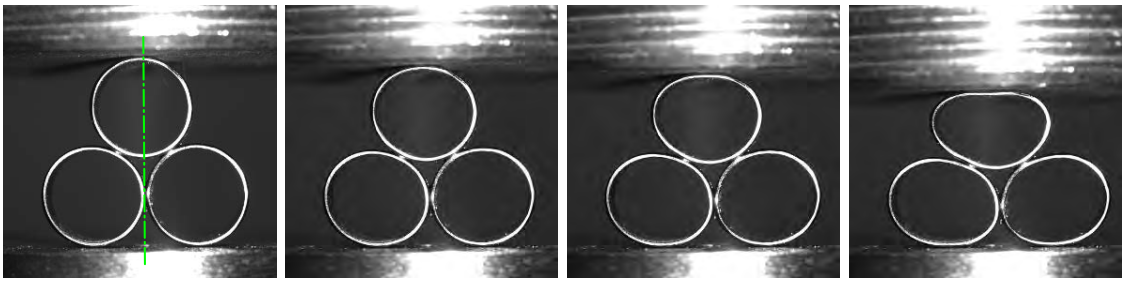

(a) (b) (c) (d)

Figure 8: Visible CCD images of a triangular sample at $T = 23\,^{\circ}\mathrm{C}$ under quasi-static compression at a loading rate of 0.1 mm/s. (a) undeformed configuration with initial length $H_0 = 10.71\,\mathrm{mm}$, (b) $\varepsilon_g = 4\,\%$, (c) $\varepsilon_g = 8\,\%$ and (d) $\varepsilon_g = 12\,\%$.

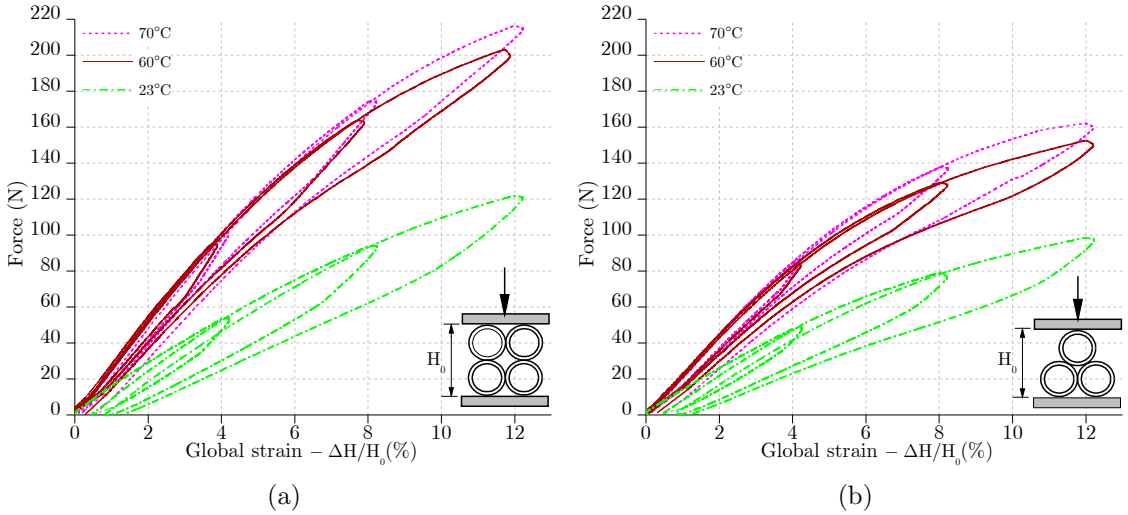

Figure 9: Load-deformation curves: (a) square sample under compression; (b) triangular sample under compression.

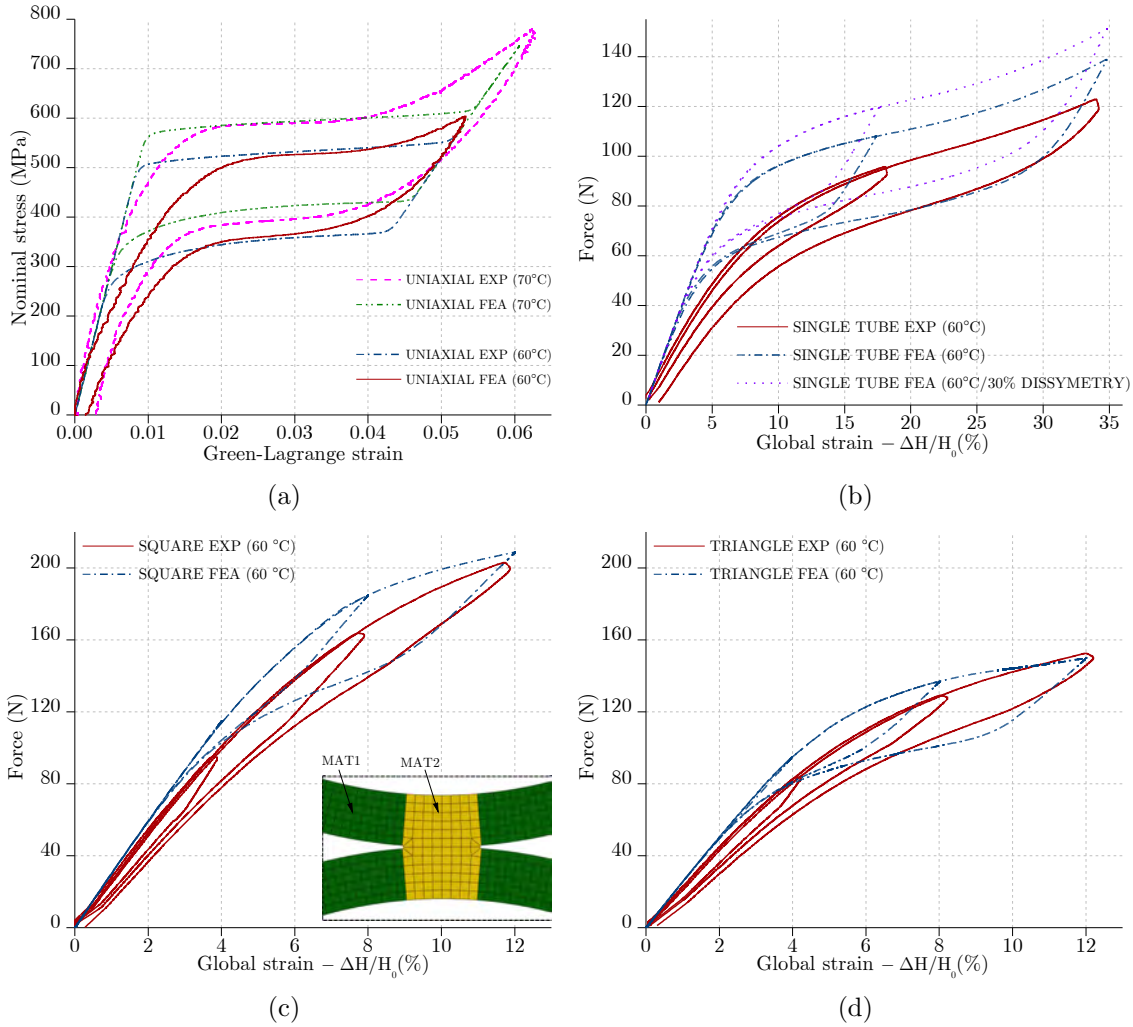

Figure 10: Comparison of experimental (EXP, red curves) and finite element analysis (FEA, blue curves) results at $T = 60\,^{\circ}\mathrm{C}$. (a) uniaxial tensile test used for parameter identification; (b) compression behavior of a single tube; (c) compression behavior of square sample with a mesh detail of the welded zone; (d) compression behavior of a triangular sample.

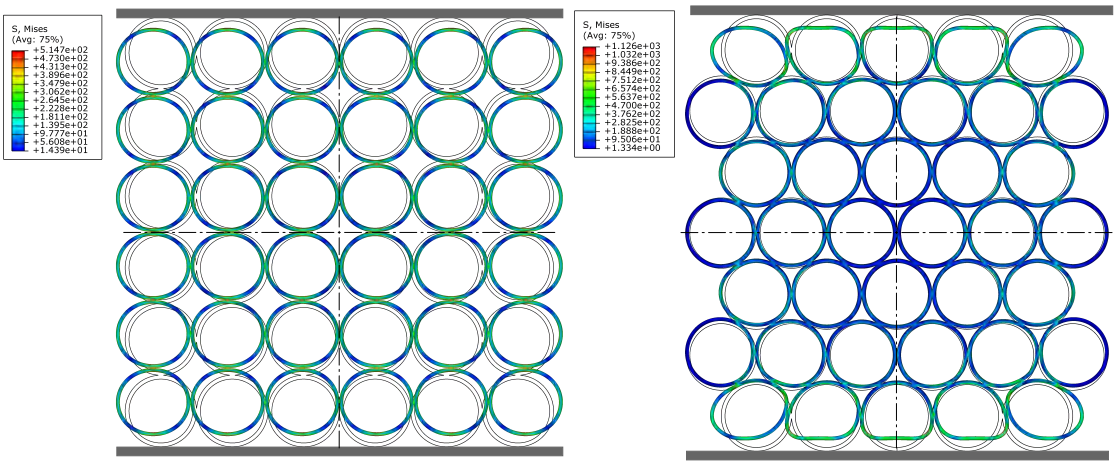

(a) (b)

Figure 11: Equivalent Mises stress field of (a) 6×6 square stacking (36 tubes) and (b) $5(4) \times 6(3)$ hexagonal stacking (38 tubes), using flat platens. The undeformed configuration is superimposed by solid lines.

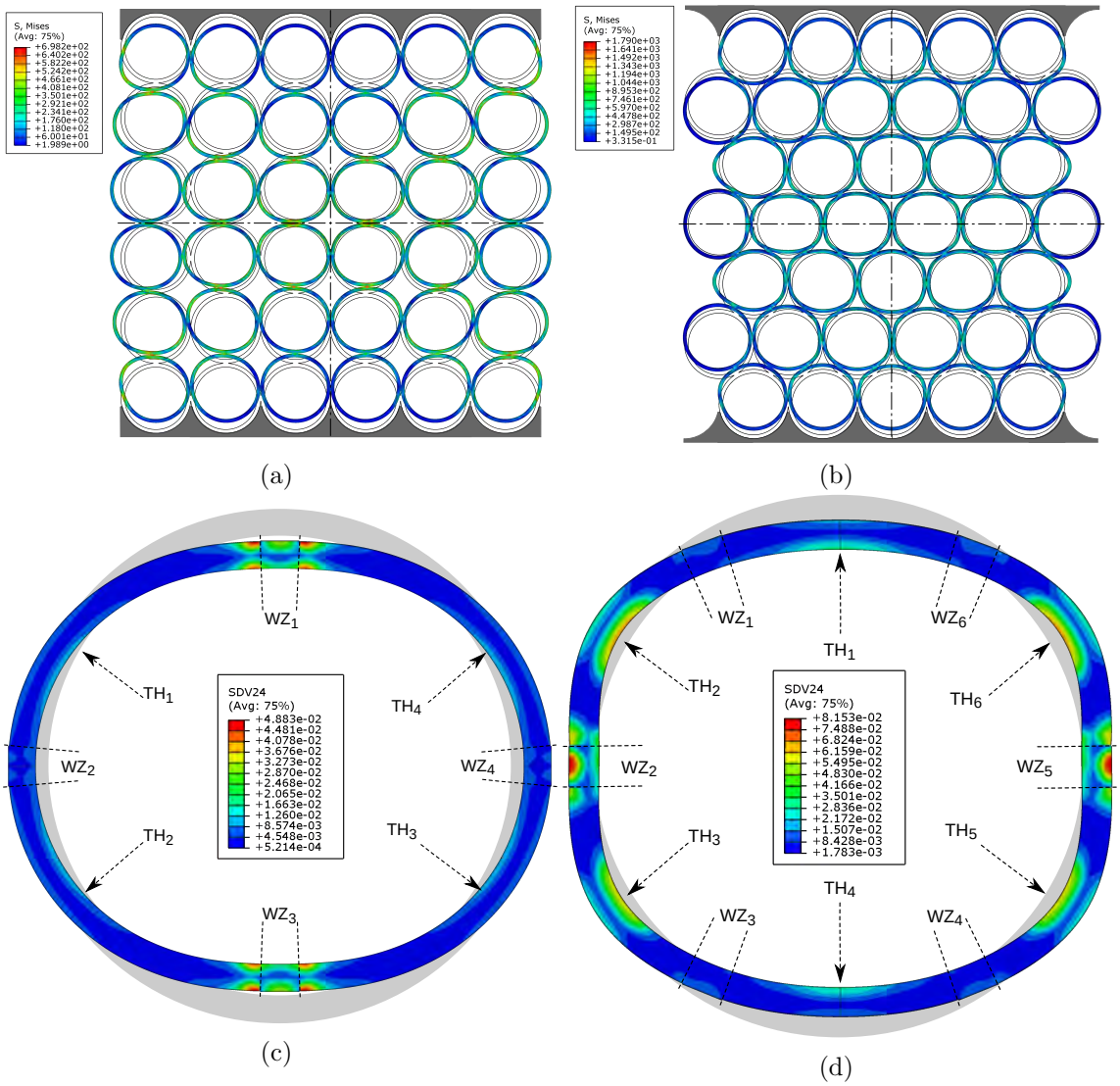

Figure 12: Finite element results of 6×6 square stacking (36 tubes) and a $5(4) \times 6(3)$ hexagonal stacking (38 tubes) using grooved platens. (a) and (b) equivalent Mises stress field. Undeformed configuration is superimposed by solid lines. (c) and (d) detail of unity tube showing the equivalent strain field for square and hexagonal stackings respectively. Welded zones (WZs) and transformation hinges (THs) are also indicated. The undeformed configuration is superimposed in gray.

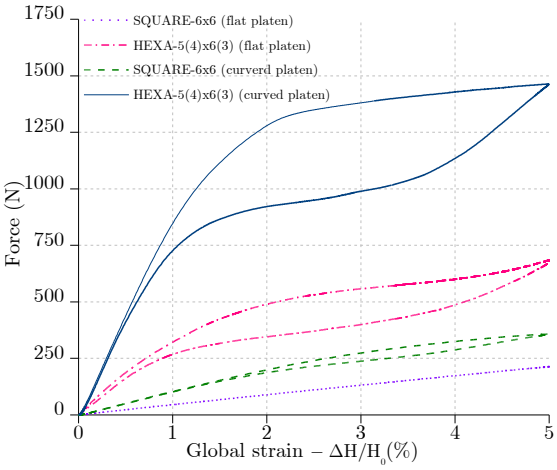

Figure 13: Compression mechanical responses of square 6×6 and hexagonal $5(4) \times 6(3)$ stackings.

Table 1: Values of the constitutive equation parameters (Auricchio's model in Abaqus UMAT)

Parameter	Unit	MAT1	MAT2
Austenite Young's modulus (E_a)	GPa	60	40
Austenite Poisson's ratio (ν_a)	-	0.33	0.33
Martensite Young's modulus (E_m)	GPa	25	20
Austenite Poisson's ratio (ν_a)	-	0.33	0.33
Transformation strain (ε^l)	-	0.04	0.05
Clausius-Clapeyron relationship ($\partial\sigma/\partial T$)	MPa/°C	6.5	6.5
Start of transformation loading (σ_l^s)	MPa	500	600
End of transformation loading (σ_l^e)	MPa	580	720
Reference temperature (T)	°C	60	60
Start of transformation unloading (σ_u^s)	MPa	390	400
End of transformation unloading (σ_u^e)	MPa	240	350

Table 2: Stress-strain points in the yield curve (Auricchio's model in Abaqus UMAT)

MAT1		MAT2	
ε_n	σ_n^p(MPa)	ε_n	σ_n^p(MPa)
0.067	1018.0	0.093	1206.9
0.071	1078.8	0.097	1253.3
0.075	1152.1	0.101	1289.1
0.087	1261.9	0.104	1308.7
0.100	1324.4	0.110	1329.0
0.112	1368.4	0.117	1354.3
0.124	1402.4	0.126	1380.1
0.136	1436.3	0.134	1400.4
0.148	1469.4	0.143	1419.4
0.177	1524.3	0.159	1449.3